European Radiology (2019) 29:6867–6879
https://doi.org/10.1007/s00330-019-06229-1

IMAGING INFORMATICS AND ARTIFICIAL INTELLIGENCE

Direct attenuation correction of brain PET images using only emission data via a deep convolutional encoder-decoder (Deep-DAC)

Isaac Shiri[1] · Pardis Ghafarian[2,3] · Parham Geramifar[4] · Kevin Ho-Yin Leung[5,6] · Mostafa Ghelichoghli[7] · Mehrdad Oveisi[7,8] · Arman Rahmim[6,9,10] · Mohammad Reza Ay[1,11]

Received: 22 February 2019 / Revised: 4 April 2019 / Accepted: 8 April 2019 / Published online: 21 June 2019

Abstract

Objective To obtain attenuation-corrected PET images directly from non-attenuation-corrected images using a convolutional encoder-decoder network.

Methods Brain PET images from 129 patients were evaluated. The network was designed to map non-attenuation-corrected (NAC) images to pixel-wise continuously valued measured attenuation-corrected (MAC) PET images via an encoder-decoder architecture. Image quality was evaluated using various evaluation metrics. Image quantification was assessed for 19 radiomic features in 83 brain regions as delineated using the Hammersmith atlas (n30r83). Reliability of measurements was determined using pixel-wise relative errors (RE; %) for radiomic feature values in reference MAC PET images.

Results Peak signal-to-noise ratio (PSNR) and structural similarity index metric (SSIM) values were 39.2 ± 3.65 and 0.989 ± 0.006 for the external validation set, respectively. RE (%) of SUV_{mean} was − 0.10 ± 2.14 for all regions, and only 3 of 83 regions depicted significant differences. However, the mean RE (%) of this region was 0.02 (range, − 0.83 to 1.18). SUV_{max} had mean RE (%) of − 3.87 ± 2.84 for all brain regions, and 17 regions in the brain depicted significant differences with respect to MAC images with a mean RE of − 3.99 ± 2.11 (range, − 8.46 to 0.76). Homogeneity amongst Haralick-based radiomic features had the highest number (20) of regions with significant differences with a mean RE (%) of 7.22 ± 2.99.

Conclusions Direct AC of PET images using deep convolutional encoder-decoder networks is a promising technique for brain PET images. The proposed deep learning method shows significant potential for emission-based AC in PET images with applications in PET/MRI and dedicated brain PET scanners.

Electronic supplementary material The online version of this article (https://doi.org/10.1007/s00330-019-06229-1) contains supplementary material, which is available to authorized users.

✉ Pardis Ghafarian
pardis.ghafarian@sbmu.ac.ir

✉ Mohammad Reza Ay
mohammadreza_ay@sina.tums.ac.ir

[1] Research Center for Molecular and Cellular Imaging, Tehran University of Medical Sciences, Tehran, Iran

[2] Chronic Respiratory Diseases Research Center, National Research Institute of Tuberculosis and Lung Diseases (NRITLD), Shahid Beheshti University of Medical Sciences, Tehran, Iran

[3] PET/CT and Cyclotron Center, Masih Daneshvari Hospital, Shahid Beheshti University of Medical Sciences, Tehran, Iran

[4] Research Center for Nuclear Medicine, Shariati Hospital, Tehran University of Medical Sciences, Tehran, Iran

[5] Department of Biomedical Engineering, Johns Hopkins University, Baltimore, MD, USA

[6] Department of Radiology and Radiological Science, Johns Hopkins University, Baltimore, MD, USA

[7] Department of Biomedical and Health Informatics, Rajaie Cardiovascular Medical and Research Center, Iran University of Medical Science, Tehran, Iran

[8] Department of Computer Science, University of British Columbia, Vancouver, BC, Canada

[9] Departments of Radiology and Physics & Astronomy, University of British Columbia, Vancouver, BC, Canada

[10] Department of Integrative Oncology, BC Cancer Research Centre, Vancouver, BC, Canada

[11] Department of Medical Physics and Biomedical Engineering, School of Medicine, Tehran University of Medical Sciences, Tehran, Iran

Key Points

- *We demonstrate direct emission-based attenuation correction of PET images without using anatomical information.*
- *We performed radiomics analysis of 83 brain regions to show robustness of direct attenuation correction of PET images.*
- *Deep learning methods have significant promise for emission-based attenuation correction in PET images with potential applications in PET/MRI and dedicated brain PET scanners.*

Keywords Positron emission tomography · Brain imaging · Artificial intelligence · Deep learning · Radiomics

Abbreviations

AC	Attenuation correction
CGAN	Conditional generative adversarial networks
CNN	Convolutional neural network
Deep-DAC	Deep direct attenuation correction
FOV	Field of view
GLCM	Gray-level co-occurrence matrix
GLRLM	Gray-level run length matrix
GLZLM	Gray-level size zone matrix
GPU	Graphics processing unit
LRE	Long-run emphasis
MAC	Measured attenuation corrected
MAE	Mean absolute error
MLAA	Maximum likelihood reconstruction of activity and attenuation
MRI	Magnetic resonance imaging
MSE	Mean squared error
NAC	Non-attenuation corrected
OSEM	Ordered subset expectation maximization
PET	Positron emission tomography
PSNR	Peak signal-to-noise ratio
RBM	Restricted Boltzmann machine
RE	Relative errors
ReLU	Rectified linear unit
RFV	Radiomic feature values
RMSE	Root mean squared error
RP	Run percentage
SRE	Short-run emphasis
SSIM	Structural similarity index metrics
SUV	Standard uptake value
SZE	Size zone emphasis
TLG	Total lesion glycolysis
TOF	Time of flight
UTE	Ultra-short echo time
VOI	Volumes of interest
ZP	Zone percentage
ZTE	Zero echo time

Introduction

Positron emission tomography (PET) has played a pivotal role in 3D non-invasive in vivo assessment of brain function [1–3]. PET provides information about biological processes, such as neurotransmitter activity in the brain [4, 5] and the presence of amyloid and tau proteins in patients with Alzheimer's disease [6, 7], and can be used for localization of disease using different measurements such as glucose, receptor binding, and cerebral blood flow [8]. Accurate quantification of uptake is an important aspect of PET imaging for neuroscience applications [9].

For neuroimaging purposes, multi-modal PET/MRI systems are increasingly utilized. Attenuation correction (AC) is a considerable challenge for such scanners, in contrast to PET/CT systems [10]. MRI measures spin properties of tissue and does not directly measure attenuation information. It is challenging to directly estimate attenuation information from MR images due to the nonlinear relationship between MR images and the attenuation patterns of tissues [11]. Different methods have been proposed to address this issue such as atlas-based [12], segmentation-based [13], and emission-based [14] methods. For atlas- and segmentation-based AC methods [15, 16], attenuation maps are generated by using T1-weighted, Dixon [13, 17], short and ultra-short echo time (UTE) [17, 18], zero echo time (ZTE) [12, 17, 19], and TWIST [20] MR sequences. For emission-based approaches, the attenuation map is directly estimated from emission data utilizing TOF information without using anatomical information [14, 21].

The latter framework (use of emission data only) also has the potential to enable construction of dedicated brain PET scanners towards more affordable amyloid or tau brain PET screening programs [22]. Different emission-based methods for AC have been proposed. An algebraic reconstruction–based technique used simultaneously reconstructed attenuation and activity maps for estimation of the attenuation coefficient from emission data [23]. This method was significantly refined with simultaneous maximum likelihood reconstruction of activity and attenuation (MLAA) [18, 24]. Different applications for AC estimation have been explored [25, 26].

Deep learning, a class of machine learning algorithms, has been shown to be well suited for processing of complex datasets in order to find patterns not explicitly recognized at the human visual level [27]. Multiple studies have begun to examine the use of deep learning architectures for cross-modality synthesis such as those for MRI cross sequences [28], MRI to CT [29], MRI and CT to PET [30], and CT to MRI [31] mappings. Specifically, some studies generated pseudo-CT from MR images to provide attenuation map for the brain region [29, 32–34]. Liu et al [35] synthesizes pseudo-

CT images from uncorrected brain 18F-FDG PET images by using a deep convolutional encoder-decoder network for AC.

In the present work, we demonstrate direct attenuation correction of PET images from non-attenuated corrected PET images using deep direct attenuation correction (Deep-DAC) to achieve quantitative brain PET images. Unlike other deep learning–based methods, the proposed method in the current study does not require anatomical information from CT or MRI. As such, it holds potential value given that cross-modality transformations can suffer from MRI and CT intra-subject mis-registration, different positioning during scans, field of view (FOV) differences between the modalities, and organ displacement during the scan [10]. It may also more readily enable quantitative application of dedicated PET-only systems. We extensively evaluate the proposed method using different image quality assessment metrics and radiomic features in different brain regions.

Material and methods

Data acquisition

Our study was approved by an Institutional Review Board (IRB). Written informed consent had been waived by our IRB committee. In total, 129 patients undergoing brain PET imaging from 2015 to 2018 were included in this study. Imaging data were collected using a GE Discovery 690 PET/CT scanner. Detailed patient demographic information is shown in Table 1. All patients fasted for at least 6 h prior to scan and were injected with 333.0 ± 62.9 MBq ^{18}F-FDG after 60-min uptake. Blood glucose levels were under 150 mg/dL (8.3 mmol/L). PET images were reconstructed using the ordered subset expectation maximization (OSEM) algorithm with 2 iterations and 24 subsets with 6.5-mm FWHM Gaussian post-smoothing. All PET images were reconstructed into 256 × 256 matrices with voxel dimensions 2.73 × 2.73 × 3.27 mm^3. All patients were scanned without contrast in spiral mode via GE VCT64 slice of GE Discovery 690 PET/CT scanner with a pitch factor 0.98:1; smart mAs; 50–60, kVp; 120 and 140, 1-s gantry rotation time, with matrix size of 512 × 512 and voxel size 1.36 × 1.36 × 3.27 mm^3.

The Deep-DAC architecture

The proposed Deep-DAC network architecture consists of encoder and decoder networks (Fig. 1) and was implemented in TensorFlow [36]. The encoder has the architecture of a convolutional network that learns feature maps from the input images. The encoder component consisted of a series of convolutional layers with 3 × 3 kernels followed by a rectified linear unit (ReLU) activation function. Batch normalization layer was then applied to stabilize and accelerate the training process. Max pooling layer with stride 2 was used for down-sampling. For each down-sampling step, the number of feature channels was doubled.

The subsequent decoder component maps the encoder output to the recovered high-resolution images. The decoder also consisted of a series of convolutional layers followed by a ReLU activation function. Transposed convolutional layers with stride 2 followed by a ReLU activation function were used for each up-sampling step where the number of feature channels was halved. Skip connections were used where the output of each layer in the encoder network was concatenated with the corresponding layer in the decoder network. This

Table 1 Demographic information of patients included in this study

Characterization		Train		Test		External validation	
		Value	%	Value	%	Value	%
No. of patient	Normal	47	51.64	10	50	10	55.55
	Epilepsy	29	31.86	7	35	8	44.45
	Cancer and metastasis	15	16.43	3	15	–	–
Gender	Male	49	53.84	12	60	11	61.11
	Female	42	45.65	8	40	7	38.39
Age (year)	Mean	32.34		32.1		34	
	Standard deviation	14.6		16.7		14.91	
	Median	29		27		32	
	Range	65		59		51	
	Minimum	10		15		16	
	Maximum	75		74		67	
	Percentiles 25	21		19		18	
	Percentiles 50	29		27		32	
	Percentiles 75	40.5		40.75		45	

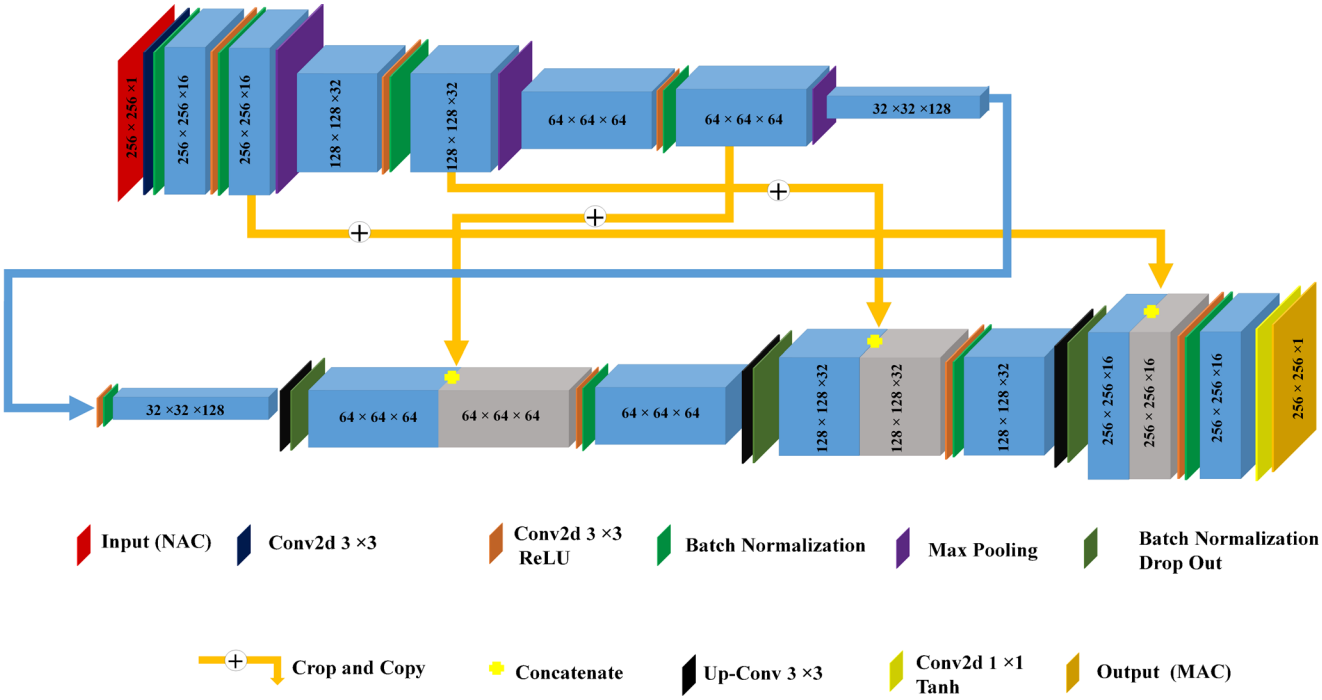

Fig. 1 The Deep-DAC architecture schematic illustration, paired encoder-decoder of Deep-DAC network and detail of each part of it

helped to address the gradient vanishing problem that occurs in deep and complex architectures.

Non-attenuation-corrected (NAC) 2D PET image slices are used as input to the encoder. The decoder then aims to reconstruct pixel-wise continuously valued measured attenuation-corrected (MAC) 2D images with a 256 × 256 matrix size. All 2D image slices for each patient were synthesized by the network in order to generate the entire 3D volume of the PET scan.

Data augmentation

We used several data augmentation methods in order to build more robust deep architectures and to avoid overfitting. Affine transformations with various sub-transforms were performed such as rotations (± 15°), translations (± 10% horizontally and vertically), shearing (± 10°), and zooming (12%) which were randomly applied to the training set images. Adding such variation to the training data helped the network to learn features that are invariant to these transformations. Data augmentation was performed only on training sets.

Training and optimization

The network was trained by minimizing a mean squared error (MSE) loss function that quantified the difference between the network-generated AC image and the MAC ground truth. The Adam optimizer with learning rate of 0.001 was used to minimize the loss function. We performed training and hyperparameter tuning of Deep-DAC with 91 patients (34,550 2D axial slices augmented; 6910 slice × 4 method + 6910 original = 34,550) for training, and 20 patients (2220 2D axial slices) for testing. To ensure network convergence, the network was trained for 1000 epochs with a mini-batch of 30 images. An epoch is defined as a single pass through the entire training set. An external validation set of 18 patients (1998 2D axial slices) was used to only evaluate the network. This external validation set was not used for fine-tuning the network hyperparameters. There was no patient overlap between the training, testing, and validation sets.

Evaluation strategy

Training, testing, and external validation sets have been strictly separated throughout all analysis steps, and further quantitative analysis was performed on external validation sets. Quality of the synthesized images was quantitatively assessed by five different metrics: mean squared error (MSE), root mean squared error (RMSE), mean absolute error (MAE), peak signal-to-noise ratio (PSNR), and structural similarity index metrics (SSIM). These metrics are defined in supplemental data.

To further evaluate quantitative performance of our proposed Deep-DAC framework, radiomic features of different brain regions were assessed. To assess quantification in the PET images, we defined 83 volumes of interest (VOI) in the brain region based on the Hammers N30R83 maximum probability atlas [37]. Image space normalization was carried prior to VOI definition. VOIs for each brain region were then exported. Further analysis was performed on original images to avoid the effect of space normalization on quantification of MAC and Deep-DAC images.

Table 2 Radiomic features (SUV, intensity, and second- and high-order texture feature) were extracted from each brain region

Radiomic feature category	Radiomic feature	Radiomic feature names
SUV	SUV	SUV_{mean}
		SUV_{max}
		Total lesion glycolysis (TLG)
First-order feature	Intensity	Q1
		Median
		Q3
		AUC
		Energy
		Entropy
		Kurtosis
Second-order texture	Gray-level co-occurrence matrix (GLCM)	Dissimilarity
		Entropy
		Energy
		Homogeneity
High-order textures	Gray-level run length matrix (GLRLM)	Run percentage (RP)
		Long-run emphasis (LRE)
		Short-run emphasis (SRE)
	Gray-level size zone matrix (GLZLM)	Size zone emphasis (SZE)
		Zone percentage (ZP)

In our work, the 83 VOIs were mapped to both Deep-DAC and reference MAC images (Supplemental Table 1). All VOIs were quantified using 19 robust radiomic features based on previous study [38] using the Pyradiomics python library [39]. Specifically, SUV, intensity, and second- and high-order texture features were extracted from the VOIs. Detailed information for these radiomic features is shown in Table 2. We determined the relative errors (RE) (%) in the radiomic feature values (RFV) between our proposed Deep-DAC and reference MAC images:

$$\mathrm{RE}\ (\%) = \frac{\mathrm{DeepDAC_{RFV}} - \mathrm{MAC_{RFV}}}{\mathrm{MAC_{RFV}}} \times 100\% \quad (1)$$

Statistical analysis

All statistical analyses were carried out by R (www.r-project.com). Paired-sample *t* tests were used for statistical analysis to compare radiomic features between Deep-DAC and CT-based AC (reference MAC) images in all 83 brain VOIs of 18 of the external validation set (1494 paired values for 19 radiomic features). The significance level was set at p value < 0.05 for all comparisons.

Results

Supplemental Figure 1 illustrates the learning curves of the training and test sets. The network converged after about 100 epochs of training. The network converged to an MSE value of $1.02e^{-4}$ and $1.69e^{-4}$ for training and test sets, respectively.

Figure 2a and b show examples of acquired NAC, MAC, and Deep-DAC images as well as bias maps between these images. Deep-DAC provided qualitatively accurate synthetic attenuation-corrected PET images of different brain regions including air, skull, and brain soft tissues.

Table 3 summarizes statistical analysis of image quality metrics, for the test and external validation sets. RMSE of $(1.19 \pm 0.5)e^{-2}$ and $(1.19 \pm 0.49)e^{-2}$ for testing and external validation set was obtained, indicating that the network was able to successfully generalize to new data in the validation set and was not overfit to the training and test sets. The PSNR and SSIM values for the test and external validation sets were 38.7 ± 3.54 and 39.22 ± 3.65 and 0.988 ± 0.006 and 0.989 ± 0.006, respectively.

Further quantitative analysis of the brain region was conducted by examining RE in the VOI. Figures 3 and 4 show the RE radiomic features and the respective *t* test p values between the Deep-DAC and MAC images for the different brain regions across all 18 subjects in the validation set. Figure 5 shows box plots for the RE of each radiomic feature in the brain. Table 4 summarizes the mean ± standard deviation and range (max–min) for the RE in all brain regions and subregions with a significant difference in RE (p value < 0.05), and more details of regions are presented in Supplemental Table 2.

The RE of SUV_{mean} was -0.1 ± 2.14 for all regions. Only three regions had a significant difference with the MAC

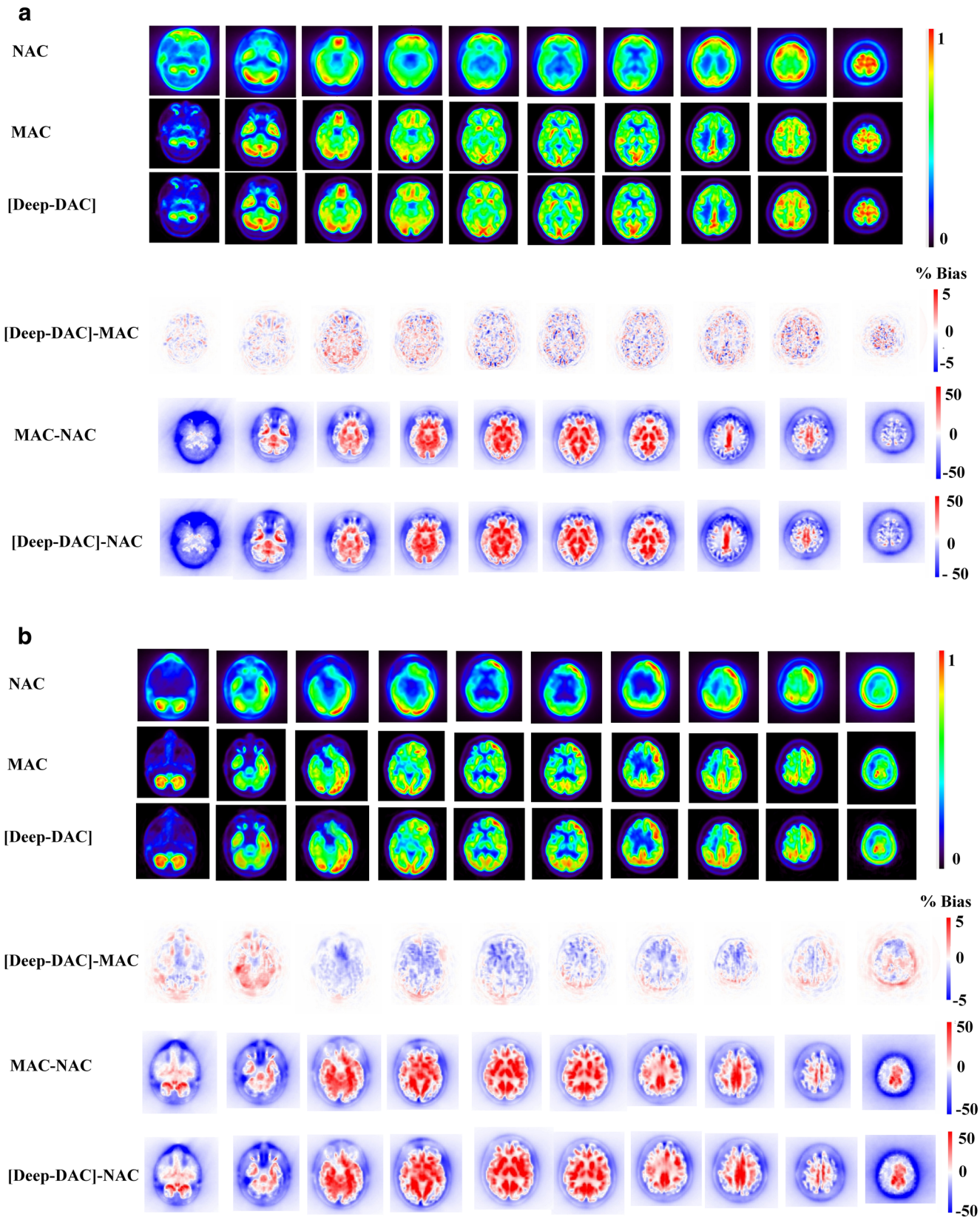

Fig. 2 *NAC*, non-attenuation correction; *MAC*, CT-based attenuation correction; *DeepDAC*, attenuation correction using Deep-DAC. **a** A 65-year-old male normal patient. **b** A 56-year-old female epilepsy patient with significant left fronto-parietal lobe and temporal lobe abnormality

Table 3 Statistical analysis of image quality metrics. *MSE* mean squared error, *RMSE* root mean squared error, *MAE* mean absolute error, *PSNR* peak signal-to-noise ratio, *SSIM* structural similarity index metrics

Dataset	MSE	RMSE	MAE	PSNR	SSIM
Test	$1.80e^{-4}$ ($0.23e^{-4}$)	$1.19e^{-2}$ ($0.5e^{-2}$)	$1.80e^{-3}$ ($0.80e^{-3}$)	38.70 (3.54)	0.988 (0.006)
Validation	$1.75e^{-4}$ ($0.17e^{-4}$)	$1.19e^{-2}$ ($0.49e^{-2}$)	$1.79e^{-3}$ ($0.83e^{-3}$)	39.22 (3.65)	0.989 (0.006)

image. The mean of difference for these regions was 0.02 with a range of − 0.83 to 1.18. SUV_{max} had a mean RE of − 3.87 ± 2.84 for all brain regions where 17 regions had a significant difference from the MAC image with a mean RE of − 3.99 and range of − 8.46 to 0.76. The radiomic feature of homogeneity (from GLCM) had the most sub-regions (20 of 83) with a significant difference between MAC and Deep-DAC with a mean RE of 7.22. In all brain sub-regions, the mean RE of homogeneity was 2.5 ± 3.65.

The left side of the putamen and the inferior frontal gyrus in left frontal lobe of the brain sub-regions exhibited significant differences in radiomic features of dissimilarity (RE%, − 11.44 and − 6.75; *p* value, 0.001 and 0.02), energy (RE%, 11.15 and 4.23; *p* value, 0.02 and 0.01), and homogeneity (RE%, 10.76 and 9.01; *p* value, 0.001 and 0.001) from GLCM. In addition, ZP (RE%, – 5.75 and − 8.65; *p* value, 0.002 and 0.03), SRE (RE%, – 0.43 and − 0.74; *p* value, 0.001 and 0.02), LRE (RE%, 2.18 and 3.30; *p* value, 0.02 and 0.02), and RP (RE%, – 0.50 and − 0.93; *p* value, 0.01 and 0.03) from GLRLM in high-order texture analysis had significant differences in these regions.

Discussion

In the present study, we propose a new approach to perform direct attenuation correction of PET images without using anatomical information. A deep convolutional encoder-decoder was developed where a NAC image was used as input to the encoder and was subsequently reconstructed by the decoder to directly produce an attenuation-corrected PET image. Further, we performed different image quality assessments with several intensity and structural measures. A total of 83 brain sub-regions for 18 patients (external validation set) were assessed quantitatively with 90 radiomic features to ensure quantitative accuracy of this approach.

RMSE of MAC and generated Deep-DAC images was (1.19 ± 0.5)e^{-2}. Ratio between the maximum possible power of a signal and noise calculated as PSNR was 38.70 ± 3.54. The SSIM between the MAC and Deep-DAC images, which measures structural similarity, was about 0.988 ± 0.006. Quantitative analysis of 83 brain regions with radiomic features shows high repeatability of the radiomic features across the proposed AC methods. Of the 1596 datapoints that were analyzed for different regions and radiomic features, only 164 datapoints had significant RE of 0.3 ± 3.2% whereas most of the data had no significant RE.

Deep learning–based approaches have been previously employed towards AC for PET images. An approach has been to generate pseudo-CT images from MRI images [32, 33, 35] and, in a recent study [34], NAC images were used to generate the pseudo-CT images for AC of PET images. Cross-modality mappings, such as from MRI to CT, involve transformation of a proton density map to an electron density map [10]. Cross-modality transformations can suffer from MRI and CT intra-subject mis-registration, different positioning during scans, field of view (FOV) differences between the modalities, and organ displacement during the scan [10]. To address these issues, we generated the attenuation-corrected images directly from the PET emission data without the need of anatomical image information.

Liu et al [32] developed and evaluated deep learning–based AC of brain PET images. They generated pseudo-CT scans from MR images and reported a dice similarity coefficient of 0.971 ± 0.005 for air, 0.936 ± 0.011 for soft tissue, and 0.803 ± 0.021 for bone. For quantitative brain analysis, mean errors of less than 1% in most brain regions were reported, though the technique was evaluated only in patients without specific neurologic abnormalities. In the present study, we included both normal and abnormal patients to provide a heterogeneous dataset. Neurologic abnormalities present in the dataset included patients with brain tumors, brain metastasis, and epilepsy. The proposed method was shown to perform well for both PET images of 10 normal and 8 abnormal patients in external validation set. Additionally, we applied data augmentation to our training set to prevent overfitting on the training set and to help build a robust deep neural network architecture.

A study performed by Spuhler et al [34] used convolutional neural network to synthesize patient-specific transmission data for PET AC neuroimages from T1-weighted MR images. Spuhler et al reported mean bias for generated transmission data − 1.06 ± 0.81% and global biases of static PET uptake − 0.49 ± 1.7%, and − 1.52 ± 0.73% for 11C-WAY-100635 and 11C-DASB scan, respectively. In our proposed method, the different regions of the brain had a mean RE of − 0.1 ± 2.14 for SUV_{mean} where 3 sub-regions had significant (p value < 0.05) differences with a mean RE of 0.02.

A recent study performed by Liu et al [35] generated pseudo-CT images from 18F-FDG NAC data of brain PET. A MAE of 111 ± 16 HU and a less than 1% average error in the quantitative analysis relative to the ground truth PET were reported. Liu et al

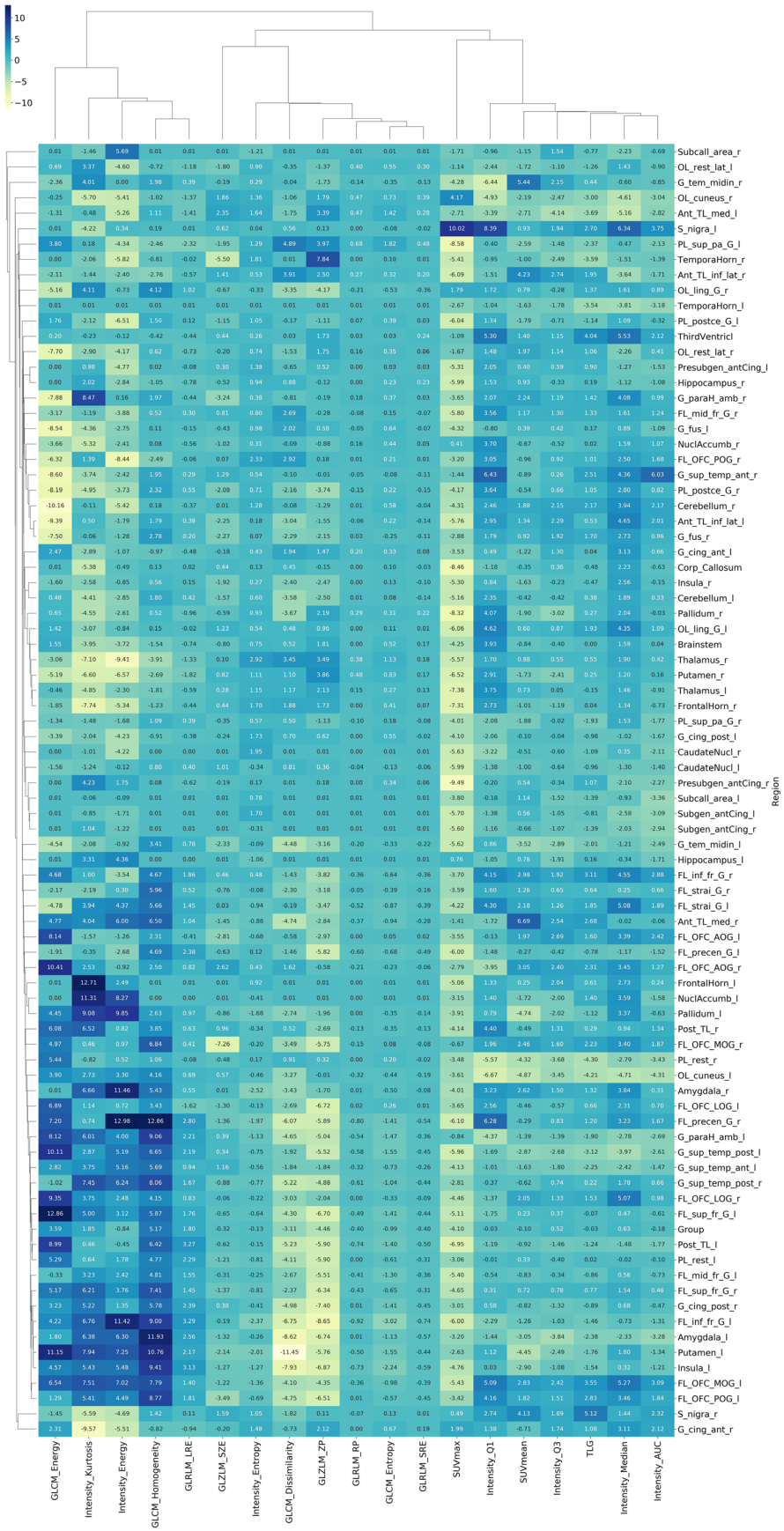

Fig. 3 Heat map depicting relative error of 19 radiomic features across 83 regions of brain in Deep-DAC and MAC

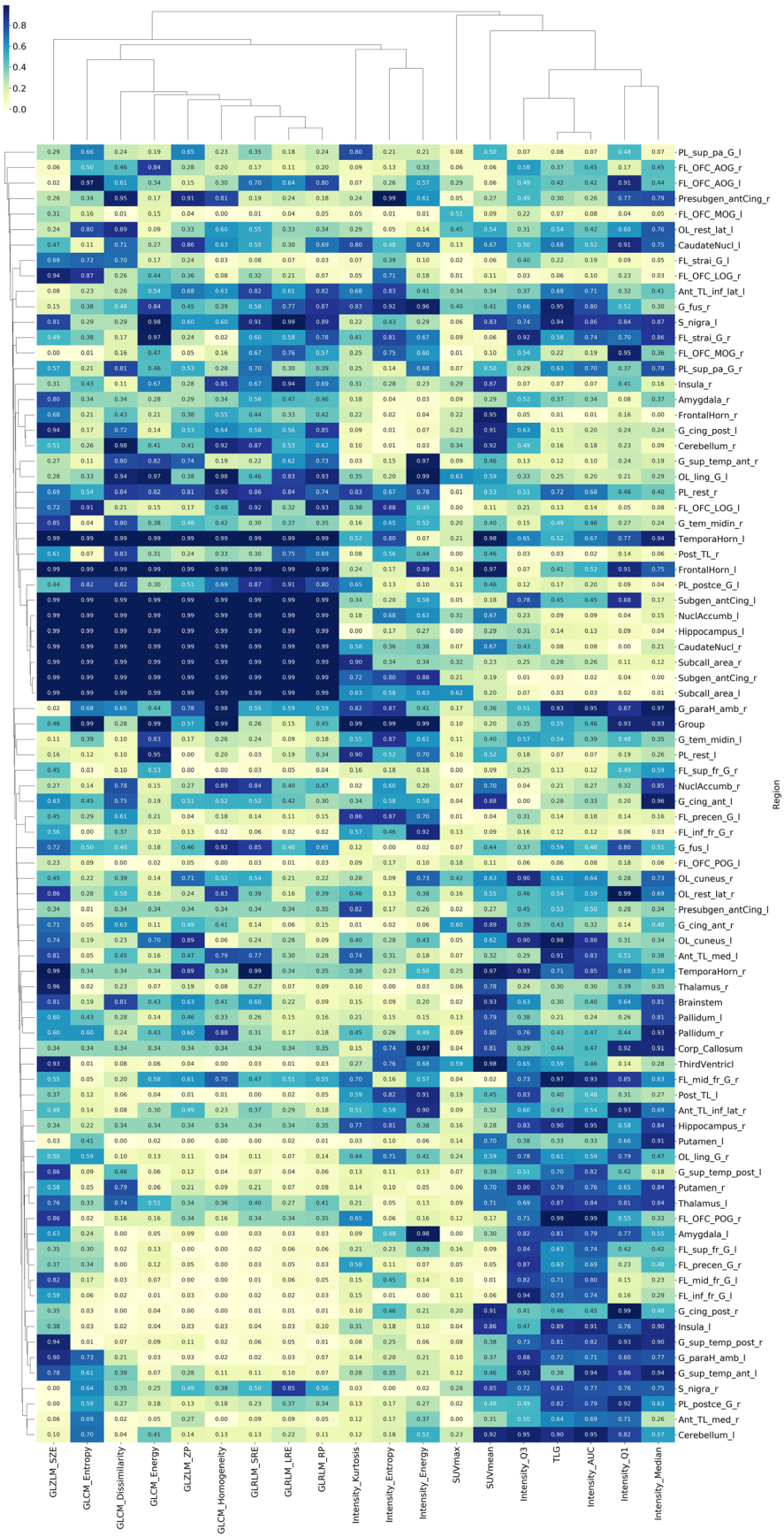

Fig. 4 Heat map depicting *p* value of *t* test in relative error of 19 radiomic features across 83 regions of brain in Deep-DAC and MAC

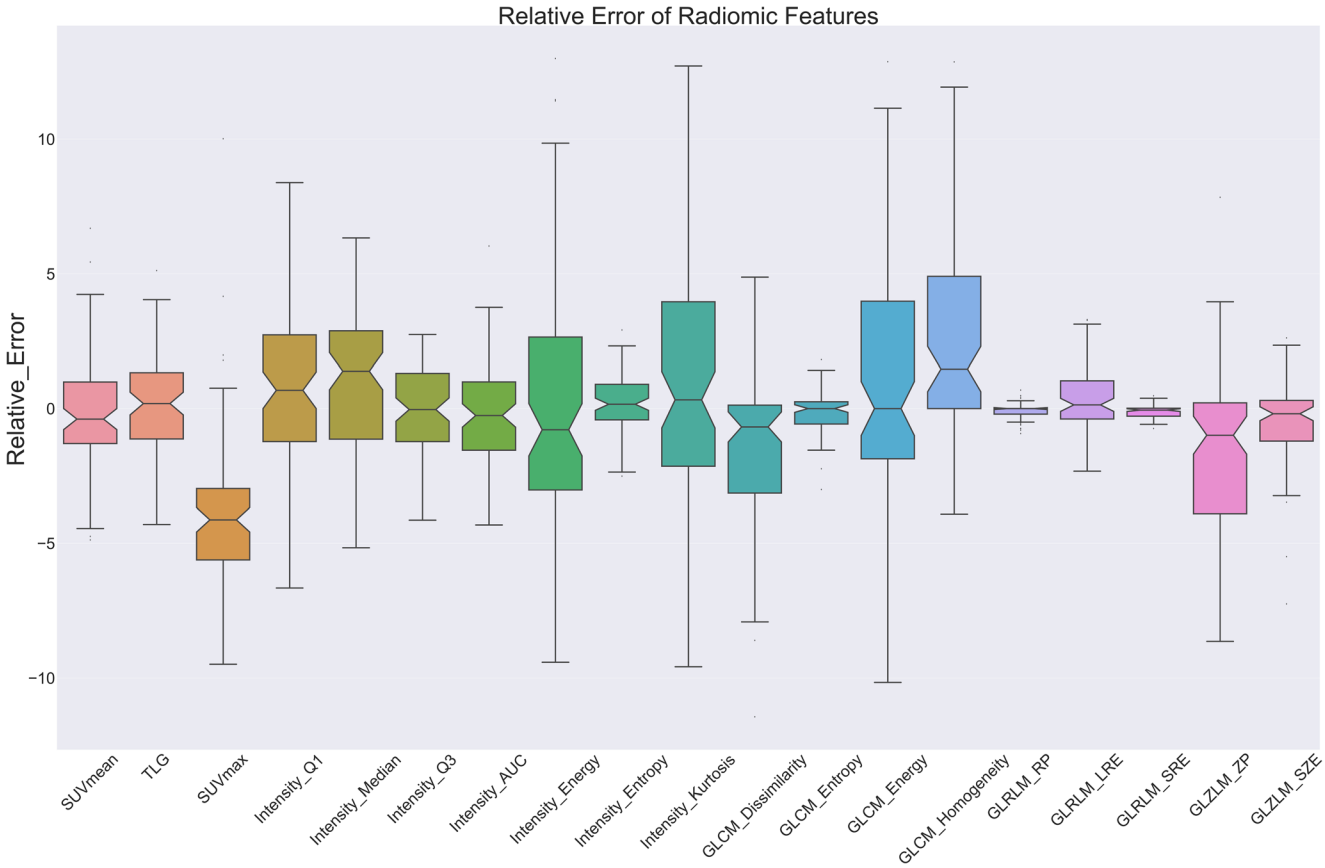

Fig. 5 Relative error box plot of radiomic features

Table 4 Summary of the mean ± std and range (Max–Min) of RE in all brain regions and the sub-region of brain with significant difference (p value < 0.05)

Radiomic features	Radiomic feature name	RE (mean ± std) All region	RE (Min–Max) All region	Mean RE Sig. region	RE Sig. region (Min–Max)	Number of region
SUV	SUV_{mean}	− 0.1 ± 2.14	− 4.88 to 6.69	0.02	− 0.83 to 1.18	3
	SUV_{max}	− 3.87 ± 2.84	− 9.49 to 10.02	− 3.99	− 8.46 to 0.76	17
	TLG	0.07 ± 1.88	− 4.3 to 5.12	− 0.61	− 1.4 to 0.3	4
Intensity	Q1	0.65 ± 2.92	− 6.66 to 8.38	0.14	− 3.21 to 5.09	4
	Median	0.91 ± 2.65	− 5.16 to 6.34	1.6	− 2.03 to 5.07	5
	Q3	− 0.09 ± 1.71	− 4.14 to 2.75	0.72	− 1.07 to 1.33	4
	AUC	− 0.26 ± 1.89	− 4.32 to 6.04	− 1.42	− 3.36 to 1.35	4
	Kurtosis	0.71 ± 4.54	− 9.58 to 12.71	− 2.16	− 9.57 to 7.94	6
	Entropy	0.16 ± 1.04	− 2.51 to 2.91	0.82	− 2.36 to 2.91	9
	Energy	0.03 ± 4.61	− 9.41 to 12.99	0.28	− 9.41 to 11.46	8
GLCM	Homogeneity	2.5 ± 3.65	− 3.92 to 12.86	7.22	− 0.42 to 12.86	20
	Energy	0.65 ± 4.96	− 10.16 to 12.87	5.43	1.29 to 11.15	6
	Entropy	− 0.18 ± 0.77	− 3.01 to 1.81	− 0.45	− 2.23 to 1.12	10
	Dissimilarity	− 1.42 ± 2.81	− 11.44 to 4.88	− 6.02	− 11.44 to − 2.66	11
GLRLM	SRE	− 0.1 ± 0.24	− 0.74 to 0.47	− 0.39	− 0.073 to 0.23	14
	LRE	0.42 ± 1.2	− 2.33 to 3.3	2.15	− 0.44 to 3.29	11
	RP	− 0.09 ± 0.3	− 0.93 to 0.69	− 0.37	− 0.92 to 0.03	11
GLZLM	SZE	− 0.49 ± 1.48	− 7.26 to 2.62	− 2.65	− 7.25 to 1.58	6
	ZP	− 1.55 ± 3.19	− 8.65 to 7.84	− 6.21	− 8.64 to 4.34	11

calculated the error as an average within the entire volume of the ROI whereas in this current study, 83 sub-regions of the brain were used to quantify 19 radiomic features. A RE of each region with significant value were present in a heat map in Figs. 3 and 4. The radiomic features of SUV_{max} (−3.87 ± 2.84), homogeneity from GLCM (2.5 ± 3.65), dissimilarity from GLCM (−1.42 ± 2.81), and ZP from GLZLM (−1.55 ± 3.19) had the highest variability in radiomic features. All other radiomic features had a RE of less than 1%. Typically, in radiomic studies, radiomic features with variances that are less than ± 5% are considered highly robust features. Such variability in radiomic features may be due to the image acquisition process, reconstruction, segmentation, or feature extraction algorithms.

Recent studies included TOF information to improve accuracy of synthesize μ-maps [40]. Mehranian et al [14] proposed a MRI-guided MLAA algorithm for emission-based AC of whole-body PET/MR images. They also compared their method with MLAA algorithms proposed by Rezaei et al [41] and Salomon et al [42]. Mehranian et al [14] reported percent error in the estimated activity of clinical FDG PET for different tissue classes: $MLAA_{rezai}$ has −10.4 ± 19, 19.9 ± 38.9, and −17.8 ± 15.5; $MLAA_{salomon}$ −2.1 ± 21.6, 18.2 ± 32.2, and −17.4 ± 14.9; $MLAA_{mehranian}$ −0.8 ± 20.2, 1.97 ± 22.9, and −5.5 ± 19.2 percent errors for fat soft tissue, lung, and bone, respectively. In the present study, the activity of 18F-FDG PET was assessed by SUV_{mean}, SUV_{max}, and TLG and had RE (%) of −0.1 ± 2.14 (−4.88 to 6.69), −3.87 ± 2.84 (−9.49 to 10.02), and 0.07 ± 1.88 (−4.3 to 5.12), respectively. The proposed deep learning–based method for AC by emission data shows less RE in soft tissue compared with previous studies.

A multi-center study performed by Ladefoged et al [43] evaluated the 11 clinically feasible brain PET/MRI AC techniques with respect to CT-based attenuation-corrected images. Ladefoged et al [43] reported a global percentage bias for vendor-implemented methods of $MR\text{-}AC_{DIXON}$ (−11.3 ± 3.5), $MR\text{-}AC_{UTE}$ (−5.7 ± 2.0); for template/atlas-based methods of $MR\text{-}AC_{SEGBONE}$ (−1.7 ± 3.6), $MR\text{-}AC_{UCL}$ (0.8 ± 1.2), $MR\text{-}AC_{MAXPROB}$ (−0.4 ± 1.6), $MR\text{-}AC_{BOSTON}$ (−0.3 ± 1.8), and $MR\text{-}AC_{ONTARIO}$ (−4.3 ± 3.6); for segmentation-based methods of $MR\text{-}AC_{CAR\text{-}RiDR}$ (−0.4 ± 1.9), $MR\text{-}AC_{MUNICH}$ (3.7 ± 2.1), and $MR\text{-}AC_{RESOLUTE}$ (0.3 ± 1.7)%; and finally for methods based on simultaneous reconstruction of attenuation and emission $MR\text{-}AC_{MLAA}$ (−1.9 ± 2.6). All 11 methods have an acceptable percentage bias (± 5% relative to CT-based image). The proposed deep learning–based method also showed the excellent performance of direct AC using PET emission data with an RE of −0.1 ± 2.35 (−3.87 to 2.5) in 19 radiomic features.

Our proposed method has several limitations. Firstly, there were a limited number of patients for training and evaluation. We used PET brain images of 111 patients in the training set. However, deep learning methods typically involve a much larger dataset that reflects all the variability between patients. To address this, we included both 62 abnormal and 67 normal patients to provide the network with a heterogeneous dataset. The network was able to generalize to new data and performed very well on the external validation set of 18 patients. However, the generalizability on to actual clinical dataset including patient with marked atrophy and skull defects must be considered. Secondly, in the current study, we used CT-based attenuation correction images as ground truth. There are several factors that make AC with CT non-ideal, including attenuation value differences in CT and PET (140 and 511 keV in CT and PET respectively), the polychromatic nature of CT beam, and the variability of the various CT image acquisition and processing steps, such as kVp, mAs, and reconstruction method. Moreover, the Deep-DAC model was only trained on 18F-FDG PET images of the brain acquired 60 min after administration. Thus, this model is only applicable for 18F-FDG PET images of the brain. To be used in other PET-based applications with different radiotracers, the network would need to be retrained on a new dataset of PET images scanned with the relevant radiotracers. Finally, the proposed Deep-DAC network performs 2D attenuation correction. The proposed method uses 2D slices as input and does not consider the trans-axial (z-axis) direction for 3D image information. In future work, we aim to extend the proposed method to a 3D network architecture in order to improve performance of our framework by incorporating 3D information.

Conclusion

The present study demonstrates applicability of a deep convolutional encoder-decoder network for direct AC of brain PET images. Quantitative analysis of 18F-FDG PET images by SUV_{mean} and SUV_{max} showed a mean RE (%) of −0.1 ± 2.14 (−4.88 to 6.69) and −3.87 ± 2.84 (−9.49 to 10.02), respectively. Deep-DAC images achieved comparable performance relative to CT-based attenuation-corrected images, as assessed using extensive quantitative analysis. Deep learning methods have significant potential to pave the road towards emission-based AC for PET images with applications in PET/MRI and dedicated brain PET imaging.

Funding This study has received funding the Tehran University of Medical Sciences under grant number 97-01-30-38001.

Compliance with ethical standards

Guarantor The scientific guarantor of this publication is Mohammad Reza Ay, PhD, Professor of Medical Physics.

Conflict of interest The authors of this manuscript declare no relationships with any companies, whose products or services may be related to the subject matter of the article.

Statistics and biometry One of the authors has significant statistical expertise. And no complex statistical methods were necessary for this paper.

Informed consent Written informed consent was waived by the Institutional Review Board.

Ethical approval Institutional Review Board approval was obtained.

Methodology
- Retrospective
- Experimental
- Performed at one institution

References

1. Catana C, Procissi D, Wu Y et al (2008) Simultaneous in vivo positron emission tomography and magnetic resonance imaging. Proc Natl Acad Sci U S A 105:3705–3710
2. Zanotti-Fregonara P, Chen K, Liow J-S, Fujita M, Innis RB (2011) Image-derived input function for brain PET studies: many challenges and few opportunities. J Cereb Blood Flow Metab 31: 1986–1998
3. Schöll M, Lockhart SN, Schonhaut DR et al (2016) PET imaging of tau deposition in the aging human brain. Neuron 89:971–982
4. Sedvall G, Farde L, Persson A, Wiesel FA (1986) Imaging of neurotransmitter receptors in the living human brain. Arch Gen Psychiatry 43:995–1005
5. Innis RB, Cunningham VJ, Delforge J et al (2007) Consensus nomenclature for in vivo imaging of reversibly binding radioligands. J Cereb Blood Flow Metab 27:1533–1539
6. Okamura N, Yanai K (2017) Brain imaging: applications of tau PET imaging. Nat Rev Neurol 13:197
7. Nordberg A, Rinne JO, Kadir A, Långström B (2010) The use of PET in Alzheimer disease. Nat Rev Neurol 6:78
8. Sarikaya I (2015) PET studies in epilepsy. Am J Nucl Med Mol Imaging 5:416
9. Lammertsma AA (2017) Forward to the past: the case for quantitative PET imaging. J Nucl Med 58:1019–1024
10. Mehranian A, Arabi H, Zaidi H (2016) Vision 20/20: magnetic resonance imaging-guided attenuation correction in PET/MRI: challenges, solutions, and opportunities. Med Phys 43:1130–1155
11. Delso G, Nuyts J (2018) PET/MRI: attenuation correction. In: Iagaru A, Hope T, Veit-Haibach P (eds) PET/MRI in Oncology. Springer, Cham, pp 53–75
12. Yang J, Wiesinger F, Kaushik S et al (2017) Evaluation of sinus/edge-corrected zero-echo-time–based attenuation correction in brain PET/MRI. J Nucl Med 58:1873–1879
13. Khateri P, Saligheh Rad H, Jafari AH et al (2015) Generation of a four-class attenuation map for MRI-based attenuation correction of PET data in the head area using a novel combination of STE/Dixon-MRI and FCM clustering. Mol Imaging Biol 17:884–892
14. Mehranian A, Zaidi H (2015) Joint estimation of activity and attenuation in whole-body TOF PET/MRI using constrained Gaussian mixture models. IEEE Trans Med Imaging 34:1808–1821
15. Akbarzadeh A, Ay MR, Ahmadian A, Alam NR, Zaidi H (2013) MRI-guided attenuation correction in whole-body PET/MR: assessment of the effect of bone attenuation. Ann Nucl Med 27: 152–162
16. Shandiz MS, Rad HS, Ghafarian P, Karam MB, Akbarzadeh A, Ay MR (2017) MR-guided attenuation map for prostate PET-MRI: an intensity and morphologic-based segmentation approach for generating a five-class attenuation map in pelvic region. Ann Nucl Med 31:29–39
17. Khateri P, Saligheh Rad H, Fathi A, Ay MR (2013) Generation of attenuation map for MR-based attenuation correction of PET data in the head area employing 3D short echo time MR imaging. Nucl Instrum Meth A 702:133–136
18. Kazerooni AF, A'arabi MH, Ay M, Saligheh Rad H (2015) Generation of MR-based attenuation correction map of PET images in the brain employing joint segmentation of skull and soft-tissue from single short-TE MR imaging modality. In: Gao F, Shi K, Li S (eds) Computational Methods for Molecular Imaging. Lecture Notes in Computational Vision and Biomechanics, vol 22. Springer, Cham, pp 139–147
19. Hope T, Tosun D, Khalighi MM et al (2017) Improvement in quantitative amyloid imaging using ZTE-based attenuation correction in PET/MRI. J Nucl Med 58:645
20. Shandiz MS, Saligheh Rad H, Ghafarian P, Yaghoubi K, Ay MR (2018) Capturing bone signal in MRI of pelvis, as a large FOV region, using TWIST sequence and generating a 5-class attenuation map for prostate PET/MRI imaging. Mol Imaging 17: 1536012118789314
21. Defrise M, Rezaei A, Nuyts J (2012) Time-of-flight PET data determine the attenuation sinogram up to a constant. Phys Med Biol 57:885
22. Sevigny J, Suhy J, Chiao P et al (2016) Amyloid PET screening for enrichment of early-stage Alzheimer disease clinical trials. Alzheimer Dis Assoc Disord 30:1–7
23. Censor Y, Gustafson DE, Lent A, Tuy H (1979) A new approach to the emission computerized tomography problem: simultaneous calculation of attenuation and activity coefficients. IEEE Trans Nucl Sci 26:2775–2779
24. Rezaei A, Defrise M, Nuyts J (2014) ML-reconstruction for TOF-PET with simultaneous estimation of the attenuation factors. IEEE Trans Med Imaging 33:1563–1572
25. Mehranian A, Zaidi H (2015) Clinical assessment of emission-and segmentation-based MR-guided attenuation correction in whole-body time-of-flight PET/MR imaging. J Nucl Med 56:877–883
26. Hemmati H, Kamali-Asl A, Ghafarian P, Ay MR (2018) Reconstruction/segmentation of attenuation map in TOF-PET based on mixture models. Ann Nucl Med 1–11, 32(7):474–484
27. LeCun Y, Bengio Y, Hinton G (2015) Deep learning. Nature 521: 436
28. Yang Q, Li N, Zhao Z, Fan X, Chang EI, Xu Y (2018) MRI image-to-image translation for cross-modality image registration and segmentation. arXiv:180106940
29. Han X (2017) MR-based synthetic CT generation using a deep convolutional neural network method. Med Phys 44:1408–1419
30. Ben-Cohen A, Klang E, Raskin SP et al (2018) Cross-modality synthesis from CT to PET using FCN and GAN networks for improved automated lesion detection. arXiv:180207846
31. Jin C-B, Jung W, Joo S et al (2018) Deep CT to MR synthesis using paired and unpaired data. arXiv:180510790
32. Liu F, Jang H, Kijowski R, Bradshaw T, McMillan AB (2017) Deep learning MR imaging–based attenuation correction for PET/MR imaging. Radiology 286:676–684
33. Gong K, Yang J, Kim K, El Fakhri G, Seo Y, Li Q (2018) Attenuation correction for brain PET imaging using deep neural network based on Dixon and ZTE MR images. Phys Med Biol 63(12):125011
34. Spuhler KD, Gardus J, Gao Y, DeLorenzo C, Parsey R, Huang C (2018) Synthesis of patient-specific transmission image for PET attenuation correction for PET/MR imaging of the brain using a convolutional neural network. J Nucl Med 60(4):555–560

35. Lu Y, Fontaine K, Germino M et al (2018) Investigation of sub-centimeter lung nodule quantification for low-dose PET. IEEE TRPMS 2:41–50
36. Abadi M, Barham P, Chen J et al (2016) TensorFlow: a system for large-scale machine learning. In 12th USENIX Symposium on Operating Systems Design and Implementation, pp 265–283
37. Hammers A, Allom R, Koepp MJ et al (2003) Three-dimensional maximum probability atlas of the human brain, with particular reference to the temporal lobe. Hum Brain Mapp 19:224–247
38. Shiri I, Rahmim A, Ghaffarian P, Geramifar P, Abdollahi H, Bitarafan-Rajabi A (2017) The impact of image reconstruction settings on 18F-FDG PET radiomic features: multi-scanner phantom and patient studies. Eur Radiol 27:4498–4509
39. van Griethuysen JJM, Fedorov A, Parmar C et al (2017) Computational radiomics system to decode the radiographic phenotype. Cancer Res 77:e104–e107
40. Hemmati H, Kamali-Asl A, Ghafarian P, Ay M (2018) Mixture model based joint-MAP reconstruction of attenuation and activity maps in TOF-PET. J Instrum 13:P06005
41. Rezaei A, Defrise M, Bal G et al (2012) Simultaneous reconstruction of activity and attenuation in time-of-flight PET. IEEE Trans Med Imaging 31:2224–2233
42. Salomon A, Goedicke A, Schweizer B, Aach T, Schulz V (2011) Simultaneous reconstruction of activity and attenuation for PET/MR. IEEE Trans Med Imaging 30:804–813
43. Ladefoged CN, Law I, Anazodo U et al (2017) A multi-centre evaluation of eleven clinically feasible brain PET/MRI attenuation correction techniques using a large cohort of patients. Neuroimage 147:346–359